Supplementary Information

Uplift, Thermal Unrest, and Magma Intrusion at Yellowstone Caldera

Charles W. Wicks, Wayne Thatcher, Daniel Dzurisin & Jerry Svarc

Methods

The InSAR data (S-Table 1) were parsed before modelling using a quadtree algorithm[S1,S2]. The parsed data points were used in an F-test to estimate 95% confidence limits. We modelled the NUA with three simple sources: a point source[S3], a prolate spheroid[S4,S5], and a dislocation model[S6] . The depth to the centre of the best-fit model for each of the three sources was deeper than 11 km. The model that best-fit the InSAR uplift data is a single expanding sill (S-Table 2), located near the base of the seismogenic crust, that dips slightly to the NNW (manuscript Figs. 3, 4). A prolate spheroid in the same location (~13 km by 3 km, centred a little more than 11 km deep, plunging about 26° to the NW) also provided a good fit to the data (S-Table 2), however, an F-test revealed that the better fit provided by the sill was significant at more than 99%. The geometry of the expanding sill beneath NUA was determined by fitting the data in Fig. 2A. Estimated 95% confidence limits are: dip 7-34º, depth to the top of the sill 9-16 km, maximum width ~14 km, and maximum length ~29 km. The best-fit sill has preferred dimensions of ~3 by 23 km (Fig. 3). To mitigate trade-offs between the expanding sill source and the contracting sills used to fit the data in Fig. 3A, the geometry of the expanding sill was fixed to that of the best-fit model for the uplift data in Fig. 2A and only the amount of expansion was allowed to vary. Starting models for the contracting sills used to model the source of subsidence are the sills we previously (ref. 4) used to model caldera-wide subsidence from 1993 to 1995. The difference between the geometry and location of initial and final models of the contracting sills is not significant at the 95% level. The

depth to the contracting sills beneath the caldera floor is between 6 and 14 km. The overlap of the inflating sill at NUA and the deflating sill beneath the caldera (Fig. 3) is non-physical. An inflating sill with a smaller aspect ratio would be more appropriate here.

The expanding sill model provides a very good fit to the InSAR data at NUA, but a distributed source model could be constructed in the shallow crust consistent with a hydrothermal source of deformation, which would also fit the uplift data. However, the deformation signal at NUA does not appear to be affected by the discontinuity of the caldera rim. The smooth nature of the deformation signal (Figs. 2, 3) and the highly heterogeneous nature of the overlying crust (Fig. 1) argue for a deep source such as we have modelled. The distribution of hydrothermal areas (active in the past and present, Fig. 1) is discontinuous across the slumped zone of the caldera at NUA. Together with the lack of seismicity near the caldera rim in Figure 4B this suggests the absence of a continuous hydrothermal system across the NUA.

Orbit No. of Master Image	Date of Master Image	Doppler Centroid (Hz)	Orbit No. of Slave Image	Date of Slave Image	Doppler Centroid (Hz)	Perpendicular Component of Baseline (m)	Figure Number
7410	1996-09-19	142	28452	2000-09-28	2	31	2A
27951	2000-08-24	-321	33462	2001-09-13	-385	81	2B
32460	2001-07-05	-83	37971	2002-07-25	310	9	2C
38973	2002-10-03	637	43482	2003-08-14	652	293	2D

S-Table 1. ERS-2 data used in this study.

Source	Weighted RMS misfit (mm)	RMS misfit (mm)
Sill	0.0064	3.65
Prolate Spheroid	0.0073	4.46
Point Source	0.0094	6.63

S-Table 2. Root Mean Square (RMS) misfit for three simple sources used to model the NUA interferogram data in Fig. 2A.

To evaluate the robustness of the InSAR modelling results, we perform a joint inversion of GPS data collected during campaigns by the Univ. of Utah in 1995 and 2000 (ref. 6) and InSAR data spanning the time from 1995 to 2000 (S-Fig. 1). Access to the GPS data was gained through the UNAVCO archive and processed using GIPSY/OASIS II software[S7] in an International Terrestrial Reference Frame 2000, North America fixed reference frame. The 1995-2000 interferogram is formed by stacking the 1996-2000 interferogram in Fig. 2C, and a 1995-1996 interferogram from Wicks et al.[4] then parsed (S-Fig. 1) as the 1996-2000 interferogram was above.

To perform a joint inversion of the GPS data and the InSAR data, we use the following weighting scheme, developed by Simons et al.[S8] and Fialko[S9], that is designed to balance the contribution between the two data sets. We normalize the GPS data (horizontal only, since the InSAR data provide better control on the vertical component of deformation than the GPS) and InSAR by applying a weighting vector with a sum of unity to the GPS and InSAR data sets.

$$\sum_{i=1}^{N} w_i = 1 \qquad (1)$$

For the GPS data the individual weighting is:

$$w_i = \frac{1}{\sigma_i \sum_{j=1}^{M} \frac{1}{\sigma_j}} \qquad (2)$$

where σ is the 95% confidence estimate for each measurement, and *M* is the number of horizontal measurements.

For the InSAR data the weighting vector is:

$$w_i = \frac{\sqrt{n_i}}{\sum_{j=1}^{N}\sqrt{n_j}} \qquad (3)$$

where the weighting w_i is applied to sub-sampled point *i*, n_i is the number of points in the quad-tree cell from which the value for the point is derived, and n_j is the number of points in each of the *N* quad-tree cells.

The quantity that we are minimizing is then:

$$\sum_{i=1}^{M}[\alpha w_i(o_i - c_i)]^2 + \sum_{i=1}^{N}[w_i(o_i - c_i)]^2 \qquad (4)$$

M is the number of horizontal GPS measurements and N is the number of InSAR measurements (quad-tree cells). The variable *o* is the observed value and *c* is the calculated value. The relative weighting factor α is set to one.

Using all the data shown in S-Fig. 1, the prolate spheroid source and dipping sill source still fit the data better, than a point source. Also note that in addition to the source parameters for each model, we have also inverted for a static shift parameter for the north component of GPS, the east component of GPS, and the InSAR data. With the inclusion of the GPS data, the dipping sill still fits the data better than the prolate spheroid, but the two are now indistinguishable at the 95% level. The dimensions of the best fit prolate spheroid are similar to that found in the InSAR modelling, but the favoured depth is shallower (~9 km depth) and the favoured plunge is nearly zero. The dimensions of the best-fit sill are within the 95% limits estimated for the best-fit sill model using the InSAR data alone, but two local minima are found with inclusion of the GPS data that are not

different from the narrow NW dipping sill model. One is a sill with an aspect ratio of two (length to width) that still dips shallowly to the NW, and the other is a long narrow sill that still has its long direction oriented to the NW, but dips shallowly (~5°) to the NE. In S-Figs. 1 and 2, we show comparisons between observations and calculations for the sill model that best fits the InSAR and GPS data (S-Fig. 1).

The eleven GPS stations most distal from the NUA (shown with dashed error ellipses, S-Fig. 1) are likely to be influenced by other deformation sources. We have marked measurements from the eleven distal GPS stations with red symbols and error bars in S-Fig. 2. Most of the outliers in S-Fig. 2 are red. If we exclude data from the eleven distal GPS stations in our inversion, the sill still fits the data slightly better than the prolate spheroid, but still with a difference that is insignificant at the 95% level. The main difference is that the best-fit sill model is now dipping shallower (~8°) and the sill length is over 30 km, slightly beyond the 95% interval found using only the InSAR data.

The main effect of adding the GPS data to the inversion is that the prolate spheroid source and narrow sill source are now found to be equally likely. This means that with this data we can not discern whether the mode of magma migration out of the caldera, as we have proposed, is sheet-like or pipe-like in nature.

Notes

In May 2000, Steamboat Geyser erupted after a 9-year period of inactivity. Steamboat Geyser, which has the distinction of being the geyser with the highest plume in the world (~100 m) has erupted five more times since. New thermal features have also formed, including a ~75 m line of fumaroles near Nymph Lake (Fig. 4). The near-annual disturbance in NGB was especially severe in the summer of 2003, with the eruption of Pork Chop geyser (active only as a hot spring after 1989), and near-boiling ground temperatures that led to closure of nearly half of the footpaths through NGB.

The small-scale areas of uplift in Fig. 2A are shown in higher resolution in S-Fig. 3. Drawing from the results of Hanssen et al.[20], the small-scale signals in the Norris-Mammoth corridor and the NUA for this interferogram are not likely to be a known source of "atmospheric effects". The small spatial scale and high amplitude would most likely correspond to areas of precipitation (if they were atmospheric in origin)[20]. The signals would not result from the presence of liquid water, but rather high water vapour content (resulting from partial evaporation of precipitation) beneath precipitating clouds[20]. Radar reflectivity images from NEXRAD[S10] (S-Fig. 4) show no precipitation in the entire Yellowstone area ten minutes before the data were acquired in each of the 2000 and 2001 images. Also note that the small-scale areas of uplift are only found in the areas of past or present hydrothermal activity (Fig. 1). Similar NEXRAD images from ~10 minutes before the acquisition time of data used in Fig. 2C (S-Table 1) also show no precipitation over Yellowstone, indicating the small scale large-amplitude anomalies in the Norris-Mammoth corridor in Fig. 2C are also not atmospheric in nature. Note also that the small-scale anomalies are restricted to the Norris-Mammoth corridor (Fig. 1, 2B, 3C; S-Fig. 3). The Norris-Mammoth corridor is a zone of recurrent faulting, where the only large excursion of post-caldera volcanism and hydrothermal activity takes place (Fig. 1). Of the ~40 Yellowstone interferograms spanning 1992 to 2003 we have examined, the 2000-2001 interferogram (Fig. 2B) is the only one with a string of small uplift-like features in the Norris-Mammoth corridor. This may just be coincidental, but we mention it because some may argue that the features could be caused by unusually prolific (perhaps unrealistically prolific) hydrothermal activity in the Norris-Mammoth corridor that produced localized water vapor or temperature variations.

The introduction of basaltic magma beneath the caldera could lead to rapid (even catastrophic) changes in the volcanic system. However, the presence of the partially molten rhyolitic body beneath Yellowstone would tend to stabilize associated thermal

effects. The heat of fusion for igneous rocks is over two orders of magnitude greater than the specific heat[S11]. Therefore as long as the rhyolite body is partially molten, it serves as a thermal buffer that tends to stabilize the shallow part of the volcanic system against sudden changes in temperature (*e.g.*, during intrusion of basalt near the base of the rhyolite body).

Supplementary References:

S1. Jonsson, S., Zebker, H., Segall, P. & Amelung, F. Fault slip distribution of the 1999 Mw 7.1 Hector Mine, California earthquake, estimated from satellite radar and GPS measurements. *Bull. Seism. Soc. Am.* **92**, 1377-1389 (2002).

S2. Simons, M., Fialko, Y. & Rivera, L. Coseismic deformation from the 1999 Mw 7.1 Hector Mine, California, earthquake, as inferred from InSAR and GPS observations. *Bull. Seism. Soc. Am.* **92**, 1390-1402 (2002).

S3. Mogi, K. Relations between the eruptions of various volcanoes and the deformation of the ground surfaces around them. *Bull. Earthq. Res. Inst. U. Tokyo*, **36**, 99-134 (1958).

S4. Yang, X.-M., Davis, P. M. & Dietrich, J. H. Deformation from inflation of a dipping finite prolate spheroid in an elastic half-space as a model for volcanic stressing. *J. Geophys. Res.*, **93**, 4249-4257 (1988).

S5. Fialko, Y. & Simons, M. Deformation and seismicity in the Coso geothermal area, Inyo County, California: Observations and modeling using satellite radar interferometry. J. Geophys. Res., 105, 21,781-21,794 (2000).

S6. Okada, Y. Surface deformation due to shear and tensile faults in a half-space. *Bull. Seismol. Soc. Am.*, **75**, 1135-1154 (1985).

S7. Webb, F. H., Zumberge, J. F. An introduction to GIPSY/OASIS-II, *JPL D-11088*, Jet Propul. Lab., Pasadena, Calif. (1995).

S8. Simons, M., Fialko, Y. & Rivera, L. Coseismic deformation from the 1999 Mw 7.1 Hector Mine, California, earthquake, as inferred from InSAR and GPS observations. *Bull. Seism. Soc. Am.*, **92**, 1390-1402 (2002).

S9. Fialko, Y. Probing the mechanical properties of seismically active crust with space geodesy: Study of the co-seismic deformation due to the 1992 Mw7.3 Landers (southern California) earthquake. *J. Geophys. Res.*, **109**, doi:10.1029/2003JB002756 (2004).

S10. http://www.ncdc.noaa.gov/oa/radar/radarresources.html

S11. Williams, H. &. McBirney, A. R. *Volcanology*, Freeman Cooper and Co. San Francisco, California, USA (1979), p397.

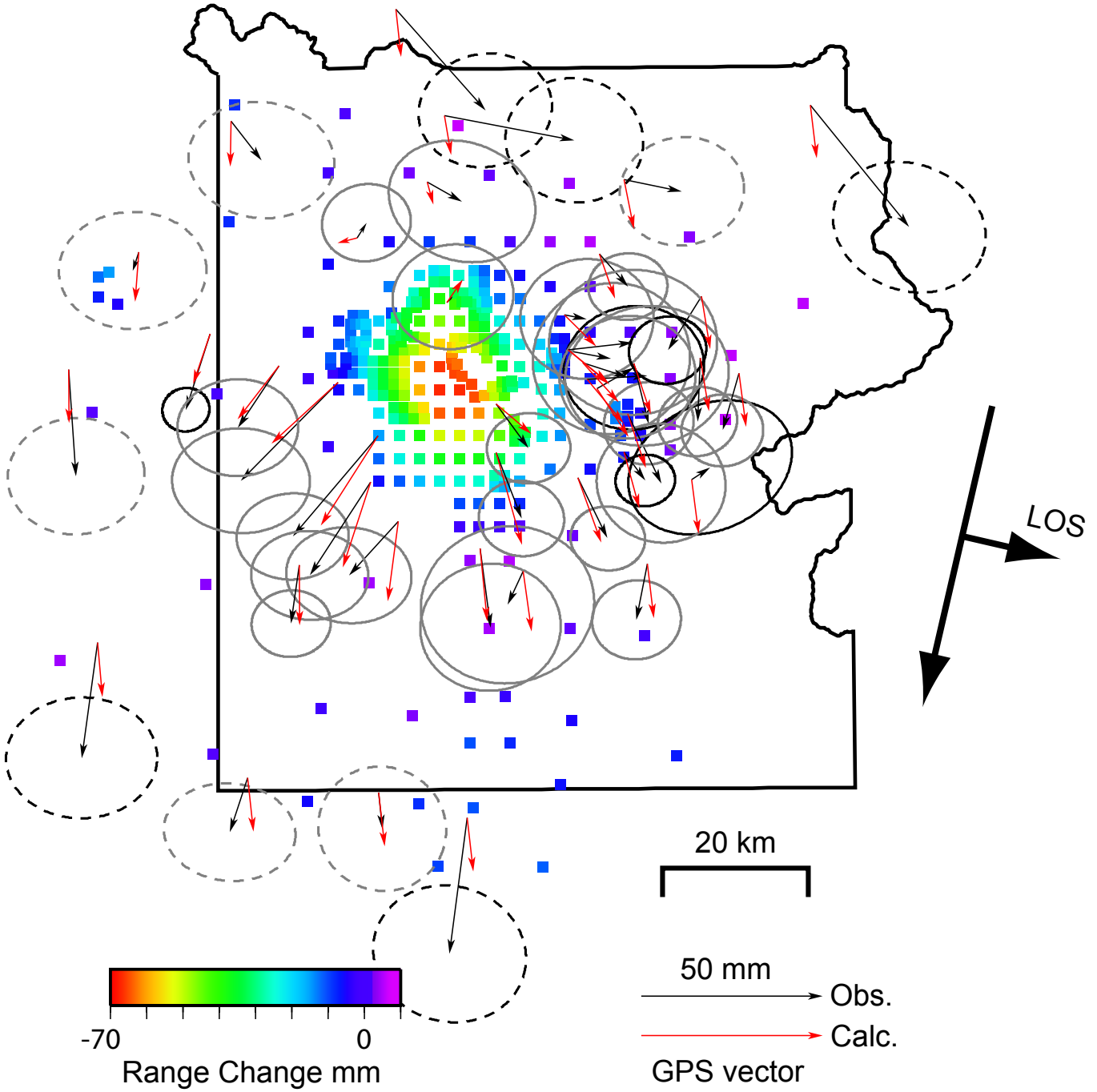

S-Figure 1. The colored squares are data parsed from an unwrapped interferogram formed by stacking the interferogram in Fig. 2A and an August 1995 to September 1996 interferogram used in Wicks et al.[4]. GPS vectors from Univ. of Utah GPS campaigns in 1995 and 2000 (ref. 6) are shown in black with 95% confidence ellipses. The red vectors show the calculated displacement from the model that best fits GPS and InSAR data (a long narrow sill). Black ellipses show where the calculated values do not fall within the 95% ellipses and gray ellipses show where the calculated values do fall within the 95% ellipses. The dashed ellipses are refered to in S-Fig. 2. The arrow labeled "LOS" shows the line-of-sight direction to the satellite, which is about 23 degrees from vertical in the center of the scene.. The arrow perpendicular to the LOS vector shows the flight track of the satellite.

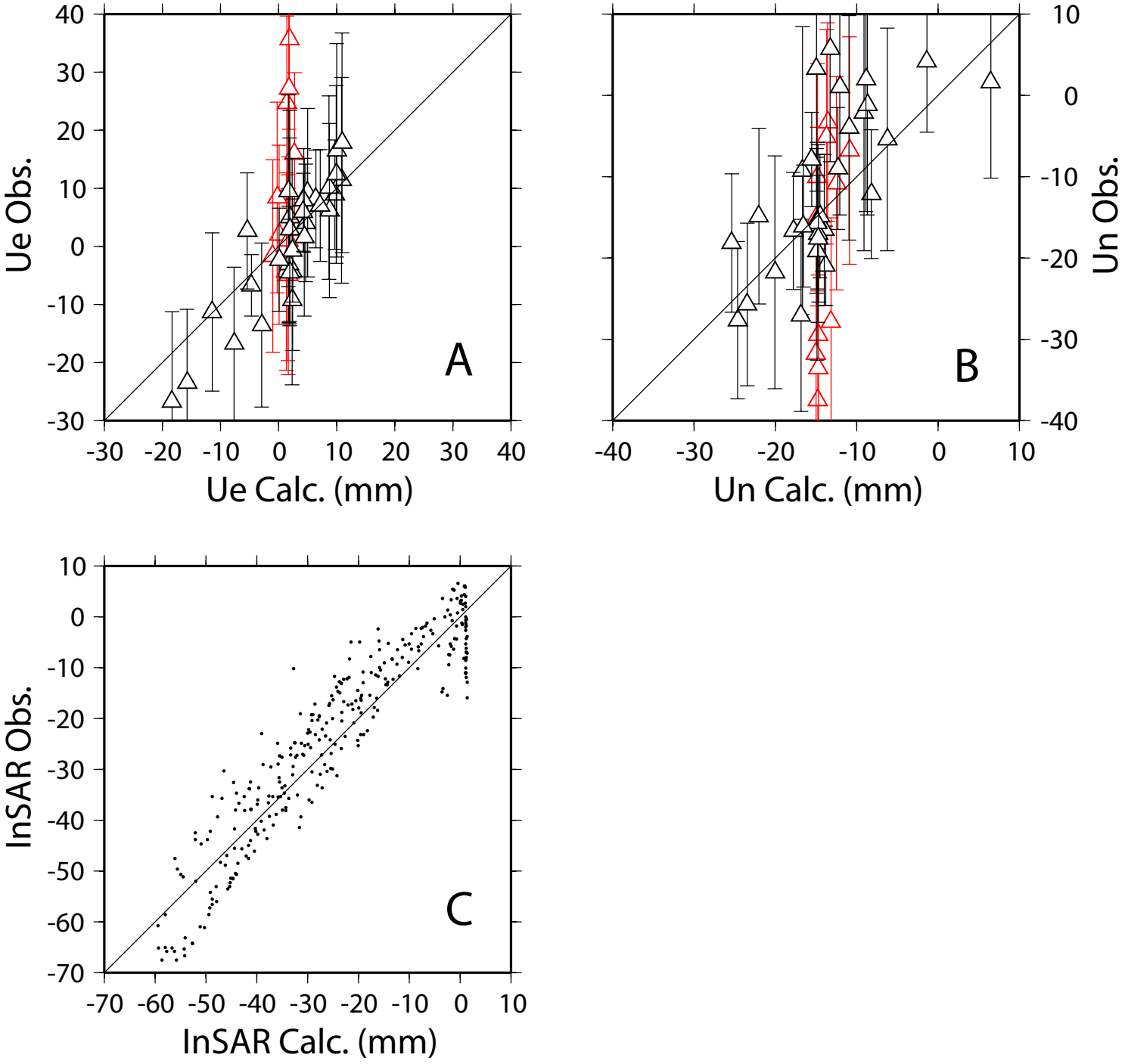

S-Figure 2. A comparison of the observed data and the calculated values for the best-fit sill model found from a joint inversion of the GPS and InSAR data. If the fit to the data was perfect, all points would fall on the diagonal lines. The red symbols and error bars in A and B correspond to the GPS stations with dashed ellipses in S-Fig. 1. **A.** The east-west component of GPS. **B.** The north-south component of GPS measurments. **C.** 1995-2000 InSAR data.

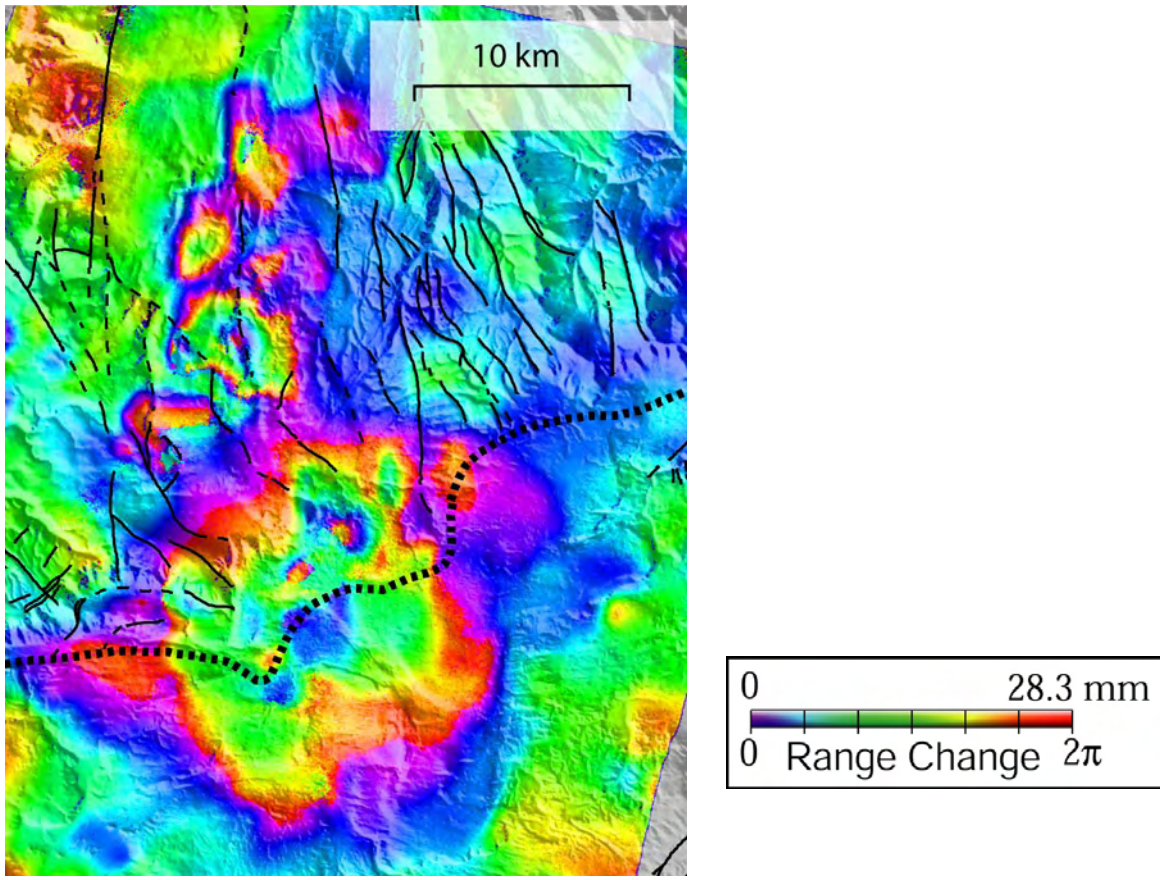

S-Figure 3. A high-resolution blow-up of the interferogram in Fig. 2B . This better shows the uplift at NUA and the small-scale areas of uplift in the Norris Mammoth corridor. Faults active in the Quaternary are marked with Black lines and the approximate caldera rim is marked with a heavy black dashed line.

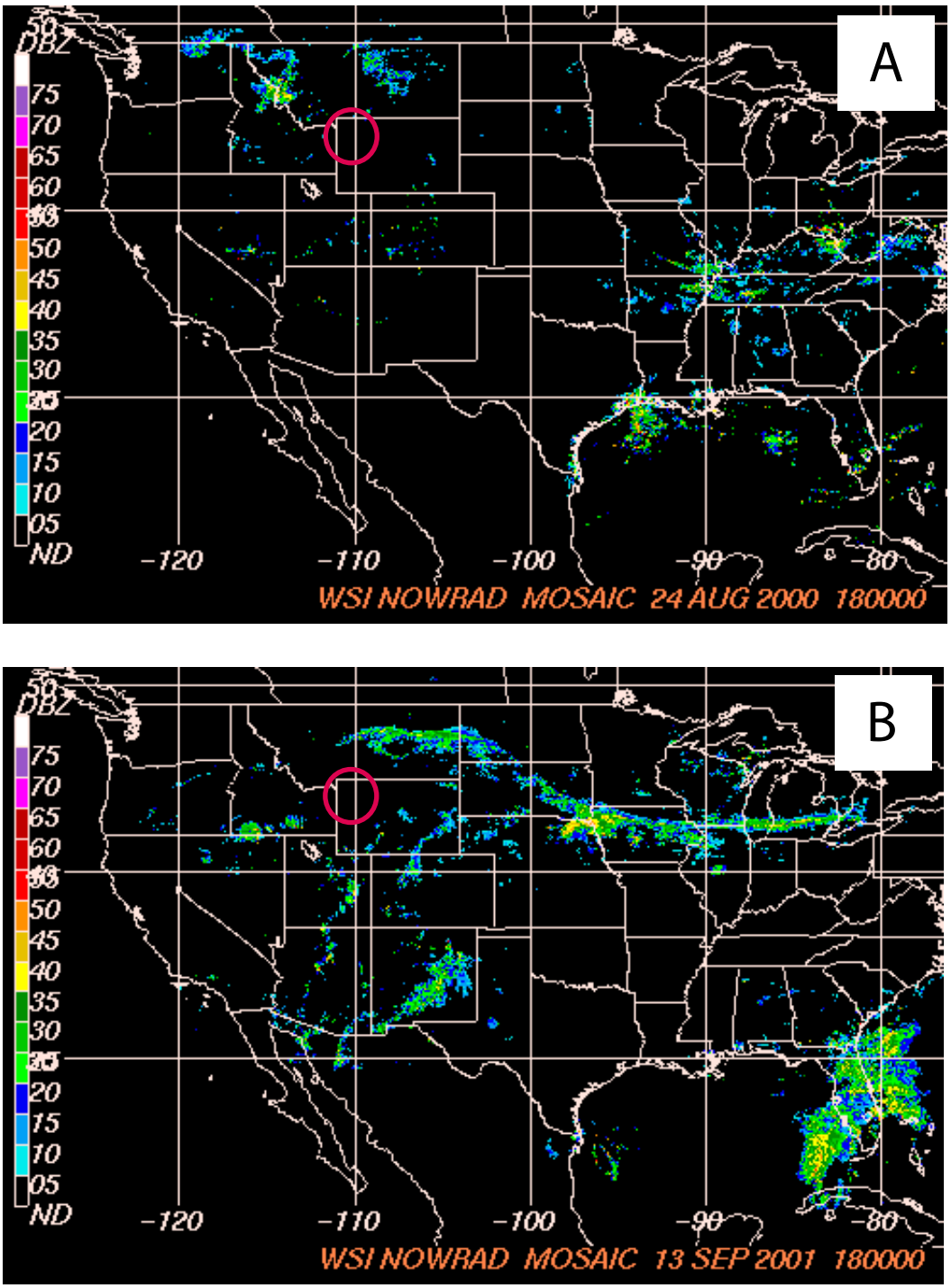

S-Figure 4. NEXRAD (Next Generation Weather Radar system) national mosaic radar reflectivity images[S9]. These two images are about 10 minutes before the ERS-2 data was acquired for the Master and Slave images used to calculate the interferogram from manuscript Fig. 2B and S-Fig. 1. They show areas of precipitation ranging from very light (light blue) to extreme (magenta to purple). The red circle surrounds Yellowstone and shows a lack of precipitation in each image. **A.** The image from ~10 minutes before the master image on Aug. 24, 2000. **B.** The image from ~10 minutes before the slave image on Sept. 13, 2001.